Accepted Manuscript

As(V) removal capacity of FeCu bimetallic nanoparticles in aqueous solutions: The influence of Cu content and morphologic changes in bimetallic nanoparticles

Pamela Sepúlveda, María A. Rubio, Samuel E. Baltazar, J. Rojas-Nunez, J.L. Sánchez Llamazares, Alejandra García García, Nicolás Arancibia-Miranda

Please cite this article as: P. Sepúlveda, M.A. Rubio, S.E. Baltazar, J. Rojas-Nunez, J.L. Sánchez Llamazares, A. García García, N. Arancibia-Miranda, As(V) removal capacity of FeCu bimetallic nanoparticles in aqueous solutions: The influence of Cu content and morphologic changes in bimetallic nanoparticles, *Journal of Colloid and Interface Science* (2018), doi: https://doi.org/10.1016/j.jcis.2018.03.113

As(V) removal capacity of FeCu bimetallic nanoparticles in aqueous solutions: The

influence of Cu content and morphologic changes in bimetallic nanoparticles

Pamela Sepúlveda[†][*], María A. Rubio[†], Samuel E. Baltazar[§], J. Rojas-Nunez[§], J.L. Sánchez

Llamazares[¥], Alejandra García García[‡], Nicolás Arancibia-Miranda[†][*]

[†] *Facultad de Química and Biología, CEDENNA, Universidad de Santiago de Chile,*

USACH, Casilla 40, Santiago C.P. 33, Chile.

[§] *Departamento de Física, CEDENNA, Universidad de Santiago de Chile, USACH, Av.*

Ecuador 3493, Santiago 9170124, Chile.

[¥] *Instituto Potosino de Investigación Científica and Tecnológica A.C., Camino a la Presa*

San José 2055 Col. Lomas 4ª, San Luis Potosí, S.L.P. 78216, México.

[‡] *Laboratorio de síntesis y modificación de nanoestructuras y materiales bidimensionales.*

Centro de Investigación en Materiales Avanzados, S.C. Alianza Norte 202, Parque PIIT,

C.P. 66628, Apodaca Nuevo León, México.

[*] *Corresponding authors. E-mail address: pamela.sepulvedaor@usach.cl (Pamela*

Sepúlveda) and nicolas.arancibia@usach.cl (Nicolás Arancibia-Miranda)

1

ABSTRACT

In this study, bimetallic nanoparticles (BMNPs) with different mass ratios of Cu and Fe were evaluated. The influence of the morphology on the removal of pollutants was explored through theoretical and experimental studies, which revealed the best structure for removing arsenate (As(V)) in aqueous systems. To evidence the surface characteristics and differences among BMNPs with different mass proportions of Fe and Cu, several characterization techniques were used. Microscopy techniques and molecular dynamics simulations were applied to determine the differences in morphology and structure. In addition, X-ray diffraction (XRD) was used to determine the presence of various oxides. Finally, the magnetization response was evaluated, revealing differences among the materials. Our cumulative data show that BMNPs with low amounts of Cu ($Fe_{0.9}Cu_{0.1}$) had a non-uniform core-shell structure with agglomerate-type chains of magnetite, whereas a Janus-like structure was observed in BMNPs with high amounts of Cu ($Fe_{0.5}Cu_{0.5}$). However, a non-uniform core-shell structure ($Fe_{0.9}Cu_{0.1}$) facilitated electron transfer among Fe, Cu and As, which increased the adsorption rate (k), capacity (q_e) and intensity (n). The mechanism of As removal was also explored in a comparative study of the phase and morphology of BMNPs pre- and post-sorption.

Keywords: Bimetallic Nanoparticles; Morphology; Molecular Dynamics; Sorption; Arsenic.

1. INTRODUCTION

Water pollution caused by inorganic contaminants is a currently a major environmental problem. Common materials such as active carbon and clays have been used as adsorbent materials. Nevertheless, these adsorbents have a low capacity and efficiency for removing metallic pollutants [1]. In this context, the use of metallic nanoparticles (NPs) as adsorbents is advantageous because NPs can adsorb and/or transform the analyte and can therefore remove larger amounts of pollutants than common materials [2]. Specifically, nanoscale zero valent iron (nZVI) has been extensively used for the decontamination of aqueous matrices due to its large reactive area and chemisorption and physisorption processes associated with surface groups, such as oxyhydroxides and hydroxyl, for the removal of lead (Pb), chromium (Cr), and arsenic (As) [3-6].

nZVI has a characteristic structure composed of an Fe^0 core covered by a shell of amorphous Fe oxide [7-10]. This structure promotes different removal processes such as adsorption, precipitation, coprecipitation, reduction, and oxidation [2, 7], resulting in the efficient removal of As and other trace elements. In particular, the removal of As using nZVI-like adsorbents [7, 11] has resulted in significant morphological changes to the nZVI surface when used in aqueous matrices or oxidizing environments [3, 11-14].

The use of nZVI for As decontamination is justified due to the strong affinity of nZVI to this analyte. As is a carcinogenic, cytotoxic, and genotoxic agent and is classified as one of the most toxic pollutants in the world [15, 16]. However, despite the great advantages of nZVI in the removal of organic and inorganic pollutants, this nanomaterial has some limitations when used in aqueous matrices and porous media, such as soil [17, 18]. These disadvantages are associated with several factors, such as the high surface energy of the NPs and corrosion processes. The former causes the formation of aggregates, in which the

NPs have a minimal surface energy and a higher stability [19]. The second problem is passivation due to the formation of Fe oxides and/or hydroxides around the particles, making the removal process slower and less effective [2, 17, 18, 20, 21].

To reduce the problems mentioned above, the combination of a second metal with nZVI to form bimetallic NPs (BMNPs) has been studied as a method for increasing the stability and reactivity relative to monometallic NPs [2, 21-27]. However, the structure adopted by these BMNPs depends on several factors, such as the preparation methods and conditions and the metal properties [28-30]. In general, the BMNP structure is classified as a core-shell (CS) or an alloy [28]. In this sense, the mass ratio of the metals in the particles as well as the presence of different compounds or species can generate structural and morphological differences in the NPs [31]. These variations produce materials with varied sizes, morphologies and compositions and, therefore, distinct reactivities [32]. Wanjala *et al.* reported that the alloying phase segregation is dependent on the size of the particles. Likewise, as mentioned above, the authors reported that BMNPs can have single-phase alloy, partial alloy or phase-segregated structures depending on the synthesis method, preparation conditions, compositions (the proportion of metals in the materials) [33] and properties of the metals, such as their surface energies, atomic size, electronegativity, oxidation potential and electronic/magnetic effects [21].

The use of BMNPs can accelerate the rates of reactions involved in the sorption processes during the removal of water pollutants [23]. This behavior has been attributed to two factors: an electrochemical process (galvanic corrosion) and the production of atomic hydrogen [23]. Electrochemical processes occur between the metals in the NPs during pollutant removal, and the effectiveness of the redox processes among all the participants depends on their reduction potentials [21]. Studies have reported that the incorporation of a

4

noble metal coating on nZVI enhances the removal reaction because noble metals have a larger reduction potential than Fe^0, which causes the reaction to be spontaneous (ΔEcell > 0) [35-36].

In particular, bimetallic particles and NPs containing Fe and Cu have been used in environmental applications because Fe is the quintessential material used for pollutant removal (high removal capacities). Likewise, Cu is a "noble metal" that protects "corrosive metals" (Fe) and has excellent antibacterial properties, making it a highly valuable material for medical and environmental (water decontamination) applications [37, 38].

With respect to environmental applications, BMNPs have been used to remove heavy metals and organic compounds, such as 1,1,1-trichloroethane, hexachlorobenzene, nitrobenzene, and p-nitrophenol [21, 39-42]. Heavy metals can be removed by different mechanisms, which mainly include adsorption and oxidation-reduction mechanisms [21]. Recently, Hu *et al.* reported that the removal of Cr(VI) using FeCu bimetallic particles occurs through electron transfer from Fe to Cu and finally to Cr(VI), which causes the oxidation of Fe(0) to Fe(II) and/or Fe(III) and Cu(0) to Cu(II), the reduction of CrO_4^{2-} to Cr^{3+}, and the formation of $(Fe_xCr_{1-x})(OH)_3$ on the surface of the material [21, 39].

The overarching goal of the present work was to evaluate the morphological changes with respect to the Fe:Cu mass ratio and the effect of this parameter on the capacity of arsenate (As(V)) removal from aqueous matrices. Thus, BMNPs with different mass ratios (0.9:0.1 and 0.5:0.5) were theoretically modeled by molecular dynamics simulations and synthesized by a chemical reduction process. The samples were characterized by magnetic response measurements, vibrating sample magnetometry (VSM), X-ray diffraction (XRD), scanning electron microscopy-energy dispersive X-ray spectroscopy (SEM-EDS), high-resolution transmission electron microscopy (HRTEM), and scanning transmission electron

microscopy (STEM). The theoretical study was used to explore different morphologies and to determine the most favorable and energetically stable structure. Furthermore, theoretical studies allowed the energetically stable structures (those with the lowest binding energy) to be correlated with the obtained experimental structures (synthesized BMNPs). Finally, the efficiency of As(V) removal by the samples was evaluated by kinetic (*first-* and *second-order* models) and isotherm (*Freundlich* and *Langmuir* models) adsorption studies. The mechanism of As(V) removal was proposed *via* a comparative study of the morphology of the BMNPs pre- and post-sorption.

2. EXPERIMENTAL SECTION

2.1 Chemicals

All chemical reagents used in the study were of analytical grade and were purchased from Merck. Solutions of $FeCl_3 \cdot 6H_2O$, $CuCl_2 \cdot 2H_2O$, 1000 mg L^{-1} As_2O_5 standard in H_2O (Titrisol), HCl, NaOH, ethanol, $NaBH_4$, and NaCl were prepared using pure water (conductivity = 18 $\mu\Omega/m$), and arsenate (As(V)) solutions of different concentrations were made by diluting the standard solution.

2.2 Synthesis of nanoparticles (NPs)

2.2.1. Nanoscale zero valent iron (nZVI) synthesis

Nanoscale Fe particles were synthesized by following the procedure described by Wang and Zhang [43], in which 60.5 $g \cdot L^{-1}$ (1.6 $mol \cdot L^{-1}$) of $NaBH_4$ and 270.2 $g \cdot L^{-1}$ (1.0 $mol \cdot L^{-1}$) of an $FeCl_3 \cdot 6H_2O$ aqueous solution were mixed at room temperature under continuous mechanical stirring. The black solid product was then separated from the solution using an ultracentrifuge (Sorvall RC-5C Plus, 9000 rpm for 10 min), washed five times with a 1:1 ethanol/water solution and degassed to remove any residual salts. The resulting material (black solid) was frozen at −18 °C and then lyophilized to obtain the final product.

2.2.2. Nanoscale zero valent copper (Cu NPs) synthesis

Nanoscale Cu particles were synthetized by adding a 1.6 $mol \cdot L^{-1}$ $NaBH_4$ aqueous solution dropwise to a 1.0 $mol \cdot L^{-1}$ $CuCl_2 \cdot 2H_2O$ aqueous solution at room temperature under continuous mechanical stirring according to the modified procedure described by Liu *et al.* [43, 44]. The resultant solution was centrifuged at 9000 rpm for 10 min, and the supernatant was replaced with ethanol/water. To avoid oxidation of the Cu NPs, ethanol/water washing was performed during purification, leading to a fine powder product after freeze-drying. The Cu NPs particles were stored in a N_2-purged desiccator.

2.2.3. FeCu bimetallic nanoparticles (FeCu BMNPs) synthesis

Synthesis of the FeCu BMNPs was carried out using Fe:Cu mass ratios of 0.9:0.1 ($Fe_{0.9}Cu_{0.1}$), 0.75:0.25 ($Fe_{0.75}Cu_{0.25}$), and 0.5:0.5 ($Fe_{0.5}Cu_{0.5}$) according to the same experimental procedure previously mentioned and proposed by Wang *et al*. [43]. This procedure involved the simultaneous reduction of both metals by $NaBH_4$, as proposed by Xiao *et al.* [41]. The solid product was then separated from the solution using an ultracentrifuge (Sorvall RC-5C Plus, 9000 rpm for 10 min), washed five times with a 1:1 ethanol/water solution and degassed to remove any residual salts. The resulting material (black solid) was frozen at −18 °C and then lyophilized to obtain the final product.

2.3. Characterization of the nanomaterials

2.3.1 Theoretical characterization: FeCu BMNP simulation

To elucidate the importance of the bimetallic cluster atomic configuration, we evaluated the stability of the FeCu BMNP clusters using theoretical calculations based on classical molecular dynamics simulations. We obtained the minimum binding energy structures and the metastable configurations of the bimetallic clusters already reported in the literature [45, 46]. Some previous reports have identified possible stable isomers for the small clusters using density functional theory (DFT) [47], but in our case, we focused on larger systems (up to 10 nm in diameter) in which the symmetry of the structure depends on the cluster size. These bimetallic clusters were simulated in a canonical ensemble using a Nöse-Hoover thermostat (NVT). The atomic interactions were modeled by a semiempirical potential using an embedded atom method (EAM) [48] in molecular dynamics LAMMPS code [49] with suitable parameters for the Fe and Cu atoms [50].

Our simulations considered atomic configurations with core-shell (CS) and polycrystalline (PL) structures that were obtained from chemical reduction synthesis and gas evaporation

techniques, respectively [45, 46]. Furthermore, we considered segregated (SG) and isolated (IS) configurations to compare our results. Initially, the structures were sintered at a rate of 0.5 K/ps from 20 K to a maximum temperature of 300-1800 K. Finally, the samples were quenched at a cooling rate of 0.25 K/ps to 0.1 K with a final equilibrium time of 0.2 ns for further analysis.

2.3.2. Magnetic, crystallographic, and superficial characterization of the NPs

Magnetic hysteresis loops were obtained as a function of the Cu concentration by vibrating sample magnetometry (VSM); the system had a magnetic moment sensitivity of 10^{-4} emu. All the results were collected at room temperature with a magnetization loop obtained as a result of an external magnetic field applied from -9 to 9 kOe.

The X-ray diffraction (XRD) analyses were performed on a Bruker D8 Advance diffractometer with a coupled Cu anode radiation source with a wavelength of 1.5418 Å at a controlled temperature (24 °C).

In addition, high-magnification images (>5000×) were acquired with a backscattered electron (BSE) detector on an FEI Nova NanoSEM 200 scanning electron microscope (SEM) operated at 15 kV in a high vacuum. Elemental analyses were performed using an INCA X-Sight energy dispersive X-ray spectrometer (EDS).

Finally, transmission electron microscopy (TEM) analyses were performed on an FEI Tecnai F30 high-resolution instrument (FEG-TEM 300 kV). Owing to the expected CS structure of the synthesized FeCu BMNPs, Z-contrast imaging and EDS studies were carried out in scanning transmission electron microscopy (STEM) mode with high-angle annular dark field (HAADF) and EDS detectors, respectively. For these TEM studies, the powder particles were dispersed in isopropyl alcohol for 5 min via ultrasonication. A few drops of the upper part of the suspension were placed on the TEM carbon-coated Cu grid.

Before TEM imaging and the elemental chemical composition studies, the grids were dried for several hours at ambient temperature.

2.4. Studies of the sorption capacities of As(V)

Batch adsorption experiments were carried out to analyze the As(V) removal capacity of the synthesized nanomaterials at room temperature (25 ± 2 °C). A 20-mL portion of the arsenic (As) solution containing 0.01 mol·L^{-1} NaCl (background electrolyte) at pH 7 was used with 50 mg of the adsorbent material. An As(V) concentration of 200 mg·L^{-1} and a stirring time of 5-180 min were used for the sorption kinetics studies. The sorption isotherms were performed over a concentration range of 1-200 mg·L^{-1} with a stirring time of 5 h. In both analyses, the samples were run in triplicate, centrifuged, filtered (0.22 μm PVDF filter, Millex-GV), and measured by inductively coupled plasma atomic emission spectroscopy (ICP-OES, Perkin Elmer 2000 DB). The As sorption capacity was determined using the following expression [51, 52]:

$$q_e = \frac{(C_0 - C_t)V}{M} \quad (1),$$

where C_o is the initial concentration of As (mg·L^{-1}), C_t is its concentration at time t or the equilibrium concentration, V is the volume (L), and M is the mass (g) of adsorbent.

2.4.1. Mathematical models of the sorption kinetics and isotherms

The experimental data obtained from the removal studies were fitted to mathematical models of the sorption kinetics and isotherms. The data obtained in this study were fitted using two kinetics models, a pseudo-first-order (PFO) model, which is described by the following equation:

$$q_t = q_e(1 - e^{-k_1 t}) \quad (2)$$

and a *pseudo-second-order* model (PSO), which is represented by the following mathematical expression:

$$q_t = \frac{q_e^2 k_2 t}{1 + q_e k_2 t} \quad (3)$$

In both models, q_e is the amount of analyte adsorbed at equilibrium ($mg \cdot g^{-1}$), q_t is the amount of adsorbate ($mg \cdot g^{-1}$) adsorbed at time t (min), and k_1 (min^{-1}) and k_2 ($mg \cdot g^{-1} \cdot min^{-1}$) are the rate constants of the PFO and PSO models, respectively [51-54].

Similarly, the results of the sorption isotherms were fitted to the *Langmuir* equation (Eq. 4)

$$q_e = \frac{q_{max} K_L C_e}{1 + K_L C_e} \quad (4)$$

and the *Freundlich* equation (Eq. 5)

$$q_e = k_F C_e^{1/n} \quad (5)$$

In both equations, q_e is the amount of analyte adsorbed per unit mass of adsorbent ($mg \cdot g^{-1}$), and C_e is the equilibrium analyte concentration ($mg \cdot L^{-1}$). In Eq. (4), q_{max} ($mg \cdot g^{-1}$) is the maximum adsorption capacity, and K_L is Langmuir's sorption constant ($L \cdot mg^{-1}$) [52-55]. For the *Freundlich* equation (Eq. 5), k_F and n are the *Freundlich* constants related to the sorption capacity and intensity, respectively [52, 56].

2. *RESULTS AND DISCUSSION*

3.1. FeCu bimetallic nanoparticle (FeCu BMNP) simulation

Fig. 1 shows the simulation results obtained for the lowest binding energy systems found for the morphological configurations of the 0.9:0.1 and 0.5:0.5 Fe:Cu ratios, which had average diameters of approximately 7 and 9 nm, respectively. The lowest energies were associated with the clusters that were minimized from the initial polycrystal (PL) configurations (see the inset in Fig. 1). If we separate the binding energy contributions of the Fe-Fe, Cu-Cu and Fe-Cu interactions, the importance of each atomic interaction can be determined. The stable atomic configuration is associated with enhanced Fe-Cu binding energies. The Fe-Fe interactions decreased, and the Cu-Cu interactions had intermediate values. However, the Fe-Cu binding energies in the final configurations show that intermediate contributions of the Fe-Cu interactions are more energetically stable, enabling the formation of semi-melted Cu clusters around the Fe core. These results were obtained with the PLs, and eventually, some regions will have Fe atoms exposed on the surface, as shown in Fig. 2 (b) and (c); this feature could be suitable for the formation of Fe oxides.

Fig. 2 shows the structural characterization of the binary clusters after energy minimization. Fig. 2 (a) depicts the partial radial distribution functions (RDFs), g(r), for the two different Cu concentrations. The Fe atoms are mainly located in the core (brown atoms in images b and c in Fig. 2), although some atoms are exposed on the surface, while their RDF (red line) shows the presence of a body-centered cubic (bcc) structure in all cases. In contrast, the Cu atoms (green atoms) are mainly located around the Fe core; their corresponding partial RDF patterns (blue lines) show a bcc structure for the 10% concentration ($Fe_{0.9}Cu_{0.1}$), and a face-centered cubic (fcc) pattern for the 50% concentration ($Fe_{0.5}Cu_{0.5}$) within with their corresponding binding energies and metals ratio condition the final

12

structure. These results suggest that at low Cu concentrations, the Cu atoms adjust to the structure of the Fe core, but as the concentration of Cu increases, the Cu atoms adopt their natural atomic structure of a fcc lattice surrounding the Fe core.

A linear atomic count of the most stable configurations was measured for both Cu concentrations, and the results are shown in Fig. 3a. At $Fe_{0.9}Cu_{0.1}$, the Fe atoms (red line) are nearly homogeneously distributed, and the Cu atoms (blue line) are noticeable at only the ends of the NPs. In contrast, at a high Cu concentration ($Fe_{0.5}Cu_{0.5}$), the structure possesses two very different regions: an Fe-rich section on the left side and a Cu-rich section on the right side, thus showing Fe-Cu segregation.

2.2. Magnetic, crystallographic, and superficial characterization of the NPs

The magnetic behavior of the synthesized BMNPs is shown in Fig. 4. From these results, we obtained the Cu concentration dependence of the magnetic saturation, which decreased as the Cu concentration increased. The lower magnetic response of nZVI relative to the other synthesized materials is associated with the presence of Fe oxide. For the Cu NPs, no magnetic response was observed for any applied magnetic field. The coercivity, Hc, and magnetic remanence were also measured. Hc decreased as the amount of Cu increased, going from 626 Oe for 0.1 Cu ($Fe_{0.9}Cu_{0.1}$) to 53 Oe for 0.5 Cu ($Fe_{0.5}Cu_{0.5}$). Finally, the remanence showed similar small values of approximately 5 emu for the 0, 0.1 and 0.5 Cu concentrations.

Fig. 5 shows the diffraction patterns obtained for the four synthesized nanomaterials. Fig. 5. (a) shows a diffractogram of nZVI, in which the characteristic peaks of Fe^0 (bcc) are seen at $2\theta = 45.23°$ and $65.25°$. For the BMNPs (Fig. 5 (b) and (c)), the signals of metallic Fe and Cu could be identified, and the Cu NPs (Fig. 5 (d)) show peaks at $2\theta = 43.27°$, $50.76°$, and $74.18°$, corresponding to Cu^0 (fcc). Peaks associated with different Cu oxides are also

13

observed in the Cu NPs at $2\theta = 36.77°$ and $61.66°$, which are attributed to cuprite (Cu_2O), and at $39.29°$, which is associated with tenorite (CuO)). For $Fe_{0.9}Cu_{0.1}$ (Fig. 5 (b)), overlap is seen between the Fe^0 and Cu^0 peaks at approximately at $2\theta = 44°$ with a considerable predominance of metallic Fe in the structure. However, as the Cu percentage in this nanomaterial increases, the hidden signal begins to appear, as seen for $Fe_{0.5}Cu_{0.5}$ (Fig. 5 (c)). In this case, the predominance of the metallic Cu signal, which exhibits behavior similar to that of the Fe signal in $Fe_{0.9}Cu_{0.1}$ but a lower intensity, is observed for $Fe_{0.75}Cu_{0.25}$ (see Fig. 1S). Furthermore, in addition to the signals of the metals, the $Fe_{0.9}Cu_{0.1}$ sample exhibits a signal at $2\theta = 35.5°$ that is attributed to magnetite, and the $Fe_{0.5}Cu_{0.5}$ sample exhibits the presence of cuprite. Therefore, this analysis establishes that these bimetallic materials were satisfactorily obtained. However, this technique cannot be used to determine the structure of the materials but instead reveals only the mineralogical phases present in the synthesized materials.

Fig. 6 shows SEM images and micrographs of nZVI (a), the BMNPs with different Fe:Cu mass ratios (b and c), and the Cu NPs (d). Fig. 6 (a) shows that the Fe NPs form a chain-like arrangement with varying NP sizes of approximately 50 and 85 nm. These chains form because Fe has the lowest energy or the most stable morphology in this structure, which is attributed to the high surface energy of the individual NPs and the physicochemical properties of the sample [57]. The low resolution of this image results from the formation of an amorphous layer around the NPs. This amorphous layer is associated with oxide formation and encapsulates the core of NPs, preventing their rapid oxidation upon exposure to the environment. Fig. 6 (b) and (c) show the BMNPs and their morphological differences according to the Fe:Cu ratio. In $Fe_{0.9}Cu_{0.1}$, the predominant chain structure corresponds to nZVI, and the presence of agglomerated zones with the emission energy of Cu was detected

14

by EDS (see Fig. 2S (b)). Similarly, a discontinuous shell attributed to the formation of an oxide layer around the bimetallic particles or to the presence of surface Cu on Fe was observed (Fig. 6 (b)). In the case of $Fe_{0.5}Cu_{0.5}$ (Fig. 6 (c)), three zones were seen. The first zone shows the presence of chains that are attributed to nZVI (red circle), the second zone shows agglomerates that are attributed to a Cu to Fe ratio of 1:1 (blue circle), and the third zone consists of sheets associated with the formation of Cu oxide on this material (yellow circle). These results are consistent with those obtained from the theoretical studies, demonstrating the formation of a CS structure and a segregated structure for $Fe_{0.9}Cu_{0.1}$ and $Fe_{0.5}Cu_{0.5}$, respectively. Similar results were obtained for the $Fe_{0.75}Cu_{0.25}$ material (see Fig. 3S (a)), which had a higher degree agglomeration than $Fe_{0.9}Cu_{0.1}$. These differences in the structure and morphology may be attributed to the surface energies of Fe and Cu, which are 2.61 $eV \cdot atom^{-1}$ and 1.37 $eV \cdot atom^{-1}$, respectively [58]. In addition, the different standard reduction potentials of the participating metals and the different Cu concentrations in the nanomaterials generate different bimetallic structures [2]. For example, Fe is likely to be at the center of the structure, forming the core of the particle, and Cu and Fe oxides are present in the shell [45, 46]. In general, the BMNPs have a complex morphology, and the complexity increases with the mass ratio of Fe to Cu. In this case, a high proportion of Cu ($Fe_{0.5}Cu_{0.5}$) causes a combination of structures to form in the material, such as segregated shell-type and intermetallic structures, alloys and/or Cu oxide sheets [59]. An image of the Cu NPs is provided in Fig. 6 (d), which is presented at a different scale than the other images due to the loss of resolution at a higher magnification. The morphology of the Cu NPs is characterized by irregular shapes with sizes greater than 100 nm, which may be a consequence of the oxidation processes that occur in this type of NP. EDS (see Fig. 2S (e)) analysis revealed the presence of Cu and Cu oxides in the material.

15

In the post-sorption studies of As(V) with these materials (Fig. 6 (e)-(h)), a morphological change associated with the presence of metal oxides was observed in the material for all cases. The SEM images clearly show the growth of sheets or the formation of a tubular morphology after As sorption and the agglomeration of individual NPs (nZVI and Cu) and BMNPs. The sheet thickness is below 250 nm in all cases [60, 61]. The increase in the amount of oxides in the samples may be attributed to the redox processes and other removal mechanisms that occur between the NPs and the pollutant, promoting a significant increase in the amount of oxygen in the structure. EDS mapping (see Fig. 2S (f-j)) identified O and As in the structures, confirming the sorption of the pollutant by the materials. In the case of the BMNPs, the $Fe_{0.9}Cu_{0.1}$ material (Fig. 6 (f)) contained a larger percentage of As and O than $Fe_{0.5}Cu_{0.5}$ (Fig. 6 (g)), which is consistent with the results observed in the removal or sorption studies. This phenomenon can be attributed to the different removal mechanisms of Fe and to the standard potential ($E°$) of Fe. Metallic Fe has a more negative $E°$ than Cu (0.341 V (Cu^{2+}/Cu^{0})), which allows easier oxidation of Fe than Cu. Both of these factors, in addition to the structure and morphology of $Fe_{0.9}Cu_{0.1}$, which has a large amount of exposed Fe on its structure, cause this material to favor the diverse mechanisms of nZVI removal, and consequently, more oxidation occurs in this material than in $Fe_{0.5}Cu_{0.5}$. In the case of the monometallic NPs, a larger percentage of As and O was found on nZVI (Fig. 6 (e)) than on the Cu NPs (Fig. 6 (h)). Similar to the previous case, this behavior may be associated with the diverse removal mechanisms and the $E°$ of Fe.

Fig. 7 shows HRTEM images of the materials, which persist in the form of NPs after As sorption. The structure of the samples observed prior to As sorption is characterized as chain-like (Fig. 7), revealing the presence of FeCu NPs (a-d) with an average diameter of 40-80 nm surrounded by amorphous oxides. After As sorption (e), the chain-like structure

16

of the $Fe_{0.9}Cu_{0.1}$ sample became wider due to the oxidation processes that occurred. The fast Fourier transform (FFT) of the images obtained of the NPs in (e) and (i) is depicted in (iii) and shows an atomic structure with patterned lines (modeled in (ii)) matching the characteristic (100) planes of the Fe bcc phase with an interplanar distance of 2.04 Å. We believe that these results confirm the formation of crystalline Fe clusters at low Cu concentrations with an increase in NP size (agglomerates) due to oxidation of the BMNPs during the redox process between the adsorbent material and As.

To study the homogeneity of the FeCu NPs, we performed STEM analysis and measured the EDS line profiles of the individual particles before and after As sorption (see Fig. 8). The concentration profiles in Fig. 8 correspond to the $Fe_{0.9}Cu_{0.1}$ (a, b, and c) and $Fe_{0.5}Cu_{0.5}$ (d, e, f and g) samples, which contain both Fe and Cu clusters. Before As sorption, Fe clusters are present in both $Fe_{0.9}Cu_{0.1}$ (a) and $Fe_{0.5}Cu_{0.5}$ (d and e), whereas Cu clusters are present in only the $Fe_{0.5}Cu_{0.5}$ (g) sample. These results also agree with our simulations performed at low and high Cu concentrations (Fig. 3) and reveal that Fe-Cu segregation occurred only at high Cu concentrations. After As sorption, the $Fe_{0.9}Cu_{0.1}$ samples (b and c) consisted of Fe NPs surrounded by Fe and Cu oxides, and As was mainly concentrated around the oxidized Fe NPs. In contrast, the $Fe_{0.5}Cu_{0.5}$ samples (f and g) consisted of highly oxidized Fe and Cu clusters with very low As concentrations around the NPs. The results for $Fe_{0.9}Cu_{0.1}$ show that the largest As concentration is achieved when the material contains more Fe and Cu (see Fig. 8 (c) and (d)). This phenomenon agrees with the observations of Lai *et al*. (2014) [22], who reported that the largest extent of pollutant degradation was achieved with FeCu bimetallic materials (compared to with nZVI). This behavior is not noticeable in $Fe_{0.5}Cu_{0.5}$ because the removal capacity of this material is lower than that of

$Fe_{0.9}Cu_{0.1}$ (results shown in the studies of the sorption capacity of As(V)), making quantification of the adsorbed analyte difficult.

2.3.   As(V) sorption capacity studies

Fig. 9 (a) shows the As sorption kinetics of the nanomaterials. The equilibrium time to reach 80% sorption with nZVI was 40 min (maximum removal), and the adsorption capacities of the remaining materials decreased in the order of $Fe_{0.9}Cu_{0.1}$ (75%), $Fe_{0.5}Cu_{0.5}$ (65%), and Cu NPs (5%) (Table 1). The decrease in the sorption capacity with the increased Cu percentage in the BMNPs can be attributed to the different morphologies (three zones) present in $Fe_{0.5}Cu_{0.5}$, as seen in the SEM images. The three zones are associated with the presence of Fe, Cu, and oxides in the material and the structural and morphological evolution of the BMNPs. In the case of $Fe_{0.9}Cu_{0.1}$, the results indicate that a larger proportion of nZVI is present on the surface of the BMNPs, and therefore, contact with the pollutant predominantly occurs through Fe^0. The monometallic NPs (nZVI) exhibit multiple analyte removal mechanisms, thus removing highs level of As [2, 7]. In contrast, with an increase in the mass proportion of Cu in the material ($Fe_{0.5}Cu_{0.5}$), As removal occurs on the nZVI as well as on the Cu NPs and Cu oxides, causing a decrease in the As removal capacity. Similar behavior was observed for $Fe_{0.75}Cu_{0.25}$ (see Fig. 4S (a)). This behavior can be attributed to the fact that the only available sorption mechanism is the reduction of As(V) to As(III) by Cu ($\Delta E = 0.22$ V) [62], which prevents sorption of this pollutant on the surface of the material and allows it to remain in solution.

After 60 min of contact, a decrease in the removal capacity occurred when Cu NPs were used as the adsorbent, and this change was less predominant in the BMNPs, which had a lower mass proportion of Cu. This trend can be attributed to the possible oxidation and morphological changes that this noble metal causes on the surface of the material [63].

18

All experimental data of this study (except those of the Cu NPs) were fitted to the pseudo-first-order (PFO) and pseudo-second-order (PSO) kinetic models, and the statistical parameters (r^2, RMSE, and χ^2) indicated that the PSO model, which is represented in Fig. 9 (a) by a dashed line, better fits the obtained data. Table 1 summarizes the PSO kinetic parameters obtained for the studied materials. The rate constant (k_2) and parameter h can be used to determine the rate of analyte adsorption on the surface of the material. The k_2 value shows that $Fe_{0.9}Cu_{0.1}$ had the fastest removal rate among the studied materials. That same behavior is reflected in the parameter h, which gives the sorption rate for the time close to zero (immediate sorption). Based on this parameter, As adsorption on $Fe_{0.9}Cu_{0.1}$ is approximately 10.3% faster than As adsorption on nZVI, which suggests that the sites of $Fe_{0.9}Cu_{0.1}$ are more accessible for adsorbing As during the first minutes of contact [64]. In addition, this behavior is consistent with that reported by O'Carrol *et al.* (2013), who stated that the second metal, in this case Cu, acts as an electronic mediator that catalyzes and increases the removal rates by BMNPs by decreasing the activation energy of the reaction [20]. However, this synergistic effect was noted for only the Fe:Cu mass ratio of 0.9:0.1 because at larger Cu concentrations, Cu NPs and Cu oxides predominate in the material, and the high level of Cu in the BMNPs does not favor the removal mechanisms of nZVI, which negatively influences the As removal capacity. A similar result was obtained for $Fe_{0.75}Cu_{0.25}$ (Table 1S).

The removal isotherms of the samples were obtained (Fig. 9 (b)), and all the materials exhibited a type *"H"* isotherm, which accounts for the high affinity of sorption that is indicated by the large initial slope [58]. All experimental data were fitted to the *Langmuir* and *Freundlich* models, and the latter represented in Fig. 9 (b) (dashed line) corresponded

to a better mathematical fit of the experimental data. The *Freundlich* model is characteristic of oxyanions that form multiple layers during the removal process [58, 62].

Table 2 shows the *Freundlich* parameters, correlation coefficient (r^2), and q_{exp} obtained for the materials, and the latter shows that the As(V) removal capacity of the $Fe_{0.9}Cu_{0.1}$ material was twice that of nZVI. The Cu NPs had the lowest removal capacity (7.83 mg·g^{-1}), and the extent of sorption decreased with an increasing percentage of Cu in the material (see Table 2S for $Fe_{0.75}Cu_{0.25}$). This phenomenon is consistent with the SEM and kinetic studies and is directly related to the structural and morphologic changes in the bimetallic material that are caused by the increase in the mass ratio of Cu in the NPs, leading to the formation of more Cu oxide sheets and Cu NPs in $Fe_{0.75}Cu_{0.25}$ than in $Fe_{0.9}Cu_{0.1}$. The predominant presence of these other Cu zones causes As to be mainly in contact with Cu instead of nZVI, and the Cu NPs possesses little affinity for this analyte.

The parameter *"n"* is related to the energy magnitude and diversity of the involved sorption processes [63] and is therefore associated with the substrate-analyte affinity or the interaction force. A value of $n > 1$ (behavior seen for nZVI, $Fe_{0.9}Cu_{0.1}$ and $Fe_{0.5}Cu_{0.5}$) represents a type-H curve, as seen in Fig. 9 (b). This behavior is attributed to the fact that the solvent minimally competes for sorption sites or that the adsorbate is a flat molecule. The same phenomenon is observed for $Fe_{0.75}Cu_{0.25}$ (Fig. 4S (b)). Table 2 shows that the Cu NPs have the largest value of this parameter despite the poor mathematical fit of the *Freundlich* model. This phenomenon may be attributed to the fact that the surface adsorption sites on the Cu NPs have a high affinity for the As(V) ions present in the solution, and these sites have a higher energy than those in nZVI and $Fe_{0.9}Cu_{0.1}$ (lower n values).

20

The sorption behavior observed in both studies can be confirmed and explained based on the results of linear mapping (Fig. 8). In $Fe_{0.9}Cu_{0.1}$, in which both metals are present in the particles (large numbers of Fe and Cu beads), a larger concentration of adsorbed As(V) is present on the material, as explained earlier. This phenomenon can be understood by considering the electrochemical processes that occur between the metals of the substrate and the pollutant.

The SEM and XRD results characterizing the materials suggest that the different morphologies and structures present in the substrates may lead to various As(V) removal mechanisms, as presented in Fig. 10.

(1)   Cu oxide layer: In aqueous and open-air systems, Cu^0 tends to be easily oxidized, and this process may be accelerated by the presence of an oxidant, such as As(V). Tenorite and/or cuprite were found on this surface, and these oxides predominantly favor the removal of the analyte through a surface adsorption mechanism [65, 66].

(2) Cu^0 layer: Based on the reports of Godoi *et al*. (2013), the main removal mechanism for Cu NPs is reduction of the analyte [67, 68], i.e., reduction of As(V) to As(III). This process involves an increase in the thickness of the oxide layer, as described earlier, which is similar to the results reported for nZVI.

(3)   Fe oxide layer and (4) Fe^0 layer: In these stages, several removal mechanisms are promoted, such as adsorption on the oxidized layer of metallic Fe; reduction of the analyte from As(V) to As(III) and, in some cases, As(0); coprecipitation to form species like simplesite ($Fe_3(AsO_4)_2$ $8H_2O$); and precipitation between the Fe oxides, Fe^0 core and As [2, 57, 69-71]. The suggested removal mechanisms involve the diffusion of As(V) from the bulk to these layers, and these phenomena occur over longer equilibration periods times.

However, in addition to the previously mentioned processes, Fig. 10 shows that catalytic and electron transfer processes occur in the bimetallic materials [32] and that Cu is responsible for initially reducing As(V) to As(III). Then, Fe completes all the other analyte removal processes, highlighting the fact that electron transfer occurs between the layers described in the figure, particularly from Fe^0 to the Cu oxide layer, which promotes removal of the pollutant.

4. CONCLUSIONS

In the present study, we examined the morphological differences between FeCu BMNPs with different mass ratios of the metals and demonstrated how these changes affect the adsorption capacity, rate, and intensity in the removal of As(V). A low proportion of Cu in the BMNPs ($Fe_{0.9}Cu_{0.1}$) favors the CS structure (discontinuous shell) and enhances the removal of As(V) relative to the $Fe_{0.5}Cu_{0.5}$ material (segregated structure). Molecular dynamics simulations were performed to study the structural morphologies of the FeCu bimetallic particles. A non-homogeneous CS structure was found to be the most stable configuration at a low Cu concentration. The Cu surrounds the Fe core, and in some areas, Fe is exposed on the surface. In addition, the atomic structure of Cu adopts a bcc structure of the core, whereas at higher Cu concentrations, a fcc structure is obtained for Cu in a segregated phase. These results suggest that Fe and Cu oxides form on the NP surface. The Fe compounds are associated with the changes in the magnetic behavior and the decreased coercivity that were observed as the Cu concentration increased. XRD characterization indicated that the Cu to Fe mass ratio affects the mineralogical phases present in the synthesized materials. Likewise, the SEM and TEM results indicated that the various Cu proportions changed the initial morphology of the NPs, which had a direct effect on the sorption capacity. The adsorption studies demonstrated that As can be removed by sorption on the FeCu BMNPs, and the best results were observed for an Fe:Cu mass ratio of 0.9:0.1 ($Fe_{0.9}Cu_{0.1}$), which yielded a non-homogeneous CS morphology. These results were consistent with the results obtained from the theoretical and characterization studies. According to the experimental results from the adsorption kinetics and isotherm studies, the PSO and *Freundlich* models, respectively, best fit the obtained data. Based on the characterization and sorption studies, the FeCu BMNPs, specifically the $Fe_{0.9}Cu_{0.1}$ BMNPs,

exhibited different removal mechanisms, such as redox reactions, adsorption, coprecipitation, and precipitation, and the catalytic or electron transfer process in this bimetallic material was determined to be the most important for As removal.

5. ACKNOWLEDGMENTS

4. REFERENCES

(1) Ihsanullah,Abbas A., M. Al-Amer A., Laoui T., J. Al-Marri M., S. Nasser M., Khraisheh M., Ali Atieh M. Review: Heavy metal removal from aqueous solution by advanced carbon nanotubes: Critical review of adsorption applications. *Sep. Purif. Technol.* **2016**, 157, 141–161.

(2) O'Carrol, D.; Sleep, B.; Krol, M., Boparai, H.; Kocur, C. Nanoscale zero valent iron and bimetallic particles for contaminated site remediation. *Adv. Water Resour*. **2013**, 51, 104–122.

(3) Manning, M.; Hunt, M.; Amrhein, C.; Yatmoff, J. Arsenic (III) and arsenic (V) reactions with zerovalent iron corrosion products. *Environ. Sci. Technol*. **2002**, 36, 5455–5461.

(4) Boparai, H.; Joseph, M.; O´carroll, D. Cadmium (Cd^{2+}) removal by nano zero valent iron: Surface analysis, effects of solution chemistry and surface complexation modeling. *Environ. Sci. Pollut. R*. **2013**, 20(9), 6210–6221.

(5) Kanel, S.; Manning, B.; Charlet, L.; Choi, H. Removal of arsenic (III) from groundwater by nano scale zero-valent iron. *Environ. Sci. Technol*. **2005**, 39, 1291–1298.

(6) Boparai, H.; Joseph, M.; O´Carroll, D. Kinetics and thermodynamics of cadmium ion removal by adsorption onto nano zerovalent iron particles. *J. Hazard. Mater*. **2011**, 186, 458–465.

(7) Yan, W.; Ramos, M.; Koel, B.; Zhang, W. As (III) sequestration by iron nanoparticles: Study of solid-phase redox transformations with X-ray photoelectron microscopy. *J. Phys. Chem. C*. **2012**, 116, 5303–5311.

(8) Li, X.; Elliott, D. W.; Zhang, W. Zero-Valent Iron Nanoparticles for Abatement of Environmental Pollutants: Materials and Engineering Aspects. Crit. Rev. Solid State Mater. Sci. **2006**, 311, 11–122.

(9) Pullin, H.; Springell, R.; Parry, S.; Scott, T. The effect of aqueous corrosion on the structure and reactivity of zero-valent iron nanoparticles. Chem. Eng. J. **2017**, 308, 568– 577.

(10) Liu, A.; Liu, J.; Han, J.; Zhang, W. Evolution of nanoscale zero-valent iron (nZVI) in water: Microscopic and spectroscopic evidence on the formation of nano- and micro-structured iron oxides. J. Hazard. Mater. **2017**, 322, 129–135.

(11) Noubactep, C. A critical review on the process of contaminant removal in Fe^0–H_2O systems. *Environ. Technol*. **2008**, 29, 909−920.

(12) Zhang, Y.; Chen, W.; Dai, C.; Zhou, C.; Zhou, X. Structural evolution of nanoscale zero-valent iron (nZVI) in anoxic Co^{2+} solution: Interactional performance and mechanism. *Sci. Rep.* **2015**, 13966 (5), 1–9.

(13) Suna, F.; Osseo-Asare, K.; Chen, Y.; Dempsey, B. Reduction of As (V) to As (III) by commercial ZVI or As (0) with acid-treated ZVI. *J. Hazard. Mater*. **2011**, 196, 311− 317.

(14) Kumar, N.; Auffan, M.; Gattacceca, J.; Rose, J.; Olivi, L.; Borschneck, D.; Kvapil, P.; Jublot, M.; Kaifas, D.; Malleret, L.; Doumenq, P.; Bottero, J. Molecular insights of oxidation process of iron nanoparticles:spectroscopic, magnetic, and microscopic evidence. *Environ. Sci. Technol.* **2014**, 48, 13888−13894.

(15) Andjelkovic, I.; Tran, D.; Kabiri, S.; Azari, S.; Markovic, M.; Losic, D. Graphene aerogels decorated with α-FeOOH nanoparticles for efficient adsorption of arsenic from contaminated waters. ACS Appl. *Mater. Interfaces* **2015**, 7, 9758−9766.

(16) Joseph, T.; Dubey, B.; McBean, E. A critical review of arsenic exposures for Bangladeshi adults. *Sci. Total Environ.* **2015**, 527-528, 540−551.

(17) Mossa Hosseini, S.; Ataie- Ashtiani, B.; Kholghi, M. Nitrate reduction by nano-Fe/Cu particles in packed column. *Desalination* **2011**, 276, 214–221.

(18) Mossa, S.; Tosco, T. Transport and retention of high concentrated nano-Fe/Cu particles through highly flow-rated packed sand column. *Water Res.* **2013**, 47, 326–338.

(19) Wu, W.; He, Q.; Jiang, C. Magnetic iron oxide nanoparticles: Synthesis and surface functionalization strategies. *Nanoscale Res. Lett*. **2008**, 3, 397–415.

(20) Shi, L.; Du, J.; Chen, Z.; Megharaj, M.; Naidu, R. Functional kaolinite supported Fe/Ni nanoparticles for simultaneous catalytic remediation of mixed contaminants (lead and nitrate) from wastewater. *J. Colloid Interf. Sci*. **2014**, 428, 302–307.

(21) Liu, W.; Qian, T.; Jiang, H. Bimetallic Fe nanoparticles: Recent advances in synthesis and application in catalytic elimination of environmental pollutants. *Chem. Eng. J*. **2014**, 236, 448–463.

(22) Lai, B.; Zhang, Y.; Chen, Z.; Yang, P.; Zhou, Y.; Wang, J. Removal of p-nitrophenol (PNP) in aqueous solution by the micron-scale iron–copper (Fe/Cu) bimetallic particles. *Appl. Catal. B Environ*. **2014**, 144, 816–830.

(23) Chun, C.; Baer, D.; Matson, D.; Amonette, J.; Peen, R. Characterization and reactivity of iron nanoparticles prepared with added Cu, Pd, and Ni. *Environ. Sci. Technol*. **2010**, 44, 5079–5085.

(24) Aslan, S.; Yalçin K.; Hanay, Ö.; Yildiz, B. Removal of tetracyclines from aqueous solution by nanoscale Cu/Fe bimetallic particle. *Desalin. Water Treat*. **2016**, 57, 14762–14773.

(25) Cui, X.; Guo, W.; Zhou, M.; Yang, Y.; Li, Y.; Xiao, P.; Zhang, Y.; Zhang, X. Promoting effect of Co in Ni_mCo_n (m + n = 4) bimetallic electrocatalysts for methanol oxidation reaction. *ACS Appl. Mater. Interfaces* **2015**, 7, 493−503.

(26) Wang, D.; Li, Y. Bimetallic Nanocrystals: Liquid-Phase Synthesis and Catalytic Applications. *Adv. Mater*. **2011**, 23, 1044–1060.

(27) Zou, Y.; Wang, X.; Khan, A.; Wang, P.; Liu, Y.; Alsaedi, A., … Wang, X. Environmental Remediation and Application of Nanoscale Zero- Valent Iron and Its Composites for the Removal of Heavy Metal Ions: A Review. Environ. Sci. Technol. 2016, 50, 7290−7304

(28) Zaleska-Medynska, A.; Marchelek, M.; Diak, M.; Grabowska, E. Noble metal-based bimetallic nanoparticles: the effect of the structure on the optical, catalytic and photocatalytic properties. *Adv. Colloid Interface Sci.* **2016**; 229, 80−107

(29) Wang, X.; Stöver, J.; Zielasek, V.; Altmann,L.; Thiel, K.; Al-Shamery, K.; Bäumer,M.; Borchert, H.; Parisi, J.; Joanna Kolny-Olesiak, J. Colloidal synthesis and structural control of PtSn Bimetallic Nanoparticles. *Langmuir* **2011**, 27, 11052–11061.

(30) Lai, B.; Zhang, Y-H.; Yuan, Y.; Chen, Z-Y.; Yang, P. Influence of Preparation Conditions on Characteristics, Reactivity, and Operational Life of Microsized Fe/Cu Bimetallic Particles. *Ind. Eng. Chem. Res.* **2014**, 53, 12295−12304.

(31) Czaplinska, J.; Sobczak, I.; Ziolek, M. Bimetallic AgCu/SBA-15 system: The effect of metal loading and treatment of catalyst on surface properties**. J. Phys. Chem. C** *2014*, 118, 12796−12810

(32) Ye, H.; Crooks, R. M. Effect of elemental ocmposition of PtPd Bimetallic Nanoparticles containing an average of 180 atoms on the kinetics of the electrochemical oxygen reduction reaction. *J. Am. Chem. Soc*. **2007**, 129, 3627−3633.

(33) Wanjala, B. N.; Luo, J.; Fang, B.; Mott, D.; Zhong, C. Gold-platinum nanoparticles: alloying and phase segregation. J. Mater. Chem. 2011, 21, 4012-4020.

(34) Zhang, Y.; Sua, Y.; Zhou, X.; Dai, C.; Keller, A. A. A new insight on the core–shell structure of zerovalent iron nanoparticles and its application for Pb(II) sequestration. *J. Hazard. Mater*. **2013**, 263, 685–693.

(35) Han, Y.; Yan, W. Bimetallic nickeleiron nanoparticles for groundwater decontamination: Effect of groundwater constituents on surface deactivation. *Water Res*. **2014**, 66, 149–159.

(36) Fu, F.; Dionysious D.; Hong, L. The use of zero- valent iron for groundwater remediation and wastewater treatment: A review. *J. Hazard. Mater*. **2014**, 267, 194–205.

(37) Chowdhury M.; Beg, M.: Maksudur, R.; Mina, M. Synthesis of copper nanoparticles and their antimicrobial performances in natural fibres. Mater. Lett. 2013, 98, 26-29.

(38) Argueta, L.; Morales, R. A.; Scougall, R. J.; Olea O. Synthesis, characterization and antibacterial activity of copper, nickel and bimetallic C-Ni nanoparticles for use in dental materials. Progress in Natural Science: Materials International, 2014, 24, 32-328.

(39) Hu, C.; Lo, S.; Liou, Y-; Hsu, Y.; Shih, K.; Lin, C. Hexavalent chromium removal from near natural water by copper–iron bimetallic particles. *Water Res*. **2010**, 44, 3101–3108.

(40) Brandsfiel, S.; Cwiertny, D.; Roberts, A.; Fairbrother, D. Influence of Copper Loading and Surface Coverage on the Reactivity of Granular Iron toward 1,1,1-Trichloroethane. *Environ. Sci. Technol*. **2006**, 40, 1485–1490.

(41) Zhu, N.; Luan, H.; Yuan, S.; Chen, J.; Wu, X.; Wang, L. Effective dechlorination of HCB by nanoscale Cu/Fe particles. *J. Hazard. Mater*. **2010**, 176, 1101–1105.

(42) Xiao, K.; Bao, Z.; Qi, X.; Wang, X.; Zhong, L., Lin, M.; Fang, K.; Sun, Y. Unsupported CuFe bimetallic nanoparticles for higher alcohol synthesis via syngas. *Catal. Commun.* **2013**, 40,154–157.

(43) Wang, C.; Zhang, W. Synthesizing Nanoscale iron Particles for Rapidand Complete Dechlorination of TCE and PCBs. *Environ. Sci. Technol*. **1997,** 31, 2154–2156.

(44) Liu, Q.; Zhou, D.; Yamamoto, Y.: Ichino, R.; Okido, M. Preparation of Cu nanoparticles with NaBH$_4$ by aqueous reduction method. *Trans. Nonferrous Met. Soc. China*. **2012**, 22, 117–123.

(45) Shafranovsky, E. A.; Petrov, Y. I.; Casas, L.; Molins, E. Structural and Mossbauer studies of aerosol FeCu nanoparticles in a wide composition range. *J. Nanopart. Res*. **2012**, 13, 4913–4928.

(46) Morales. Luckie, R.; Sanchez-Mendieta, V.; López-Castañares, R.; Arenas-Alatorre, J. Synthesis and microstructural characterization of Fe Cu Nanoparticles growth by chemical reduction. *Microsc. Microanal*. **2005**, 11, 1982–1983.

(47) Pakiari AH, Mousavi M. Influence of copper substitution on the interaction of ethylene over iron clusters: a theoretical study. *J Phys Chem A*. **2011**, 27;115(42):11796–809.

(48) Daw, M., Baskes, M. I. Embedded-atom method: Derivation and application to impurities, surfaces, and other defects in metals. *Phys. Rev. B*. **1984**, 29:12, 6443–6452.

(49) Plimton, S. Fast Parallel Algorithms for Short-Range Molecular Dynamics. *J. Comput. Phys*. **1995**, 117, 1–19.

(50) Bonny, G., Pasianot, R. C., Castin, N., Malerba, L. Ternary Fe-Cu-Ni many-body potential to model reactor pressure vessel steels: First validation by simulated thermal annealing. *Phylos. Mag*. **2009**, 89, 3531–3546.

(51) Banguella, B.; Benaissa, H. Cadmium removal from aqueous solutions by chitin: kinetic and equilibrium studies. *Water Res*. **2002**, 36, 2643–2474.

(52) Luo, J.; Luo, J.; Hu, C.; Crittenden, J.; Qu, J. Zirconia (ZrO_2) Embedded in Carbon Nanowires via Electrospinning for Efficient Arsenic Removal from Water Combined with DFT Studies. *ACS Appl. Mater. Interfaces* **2016**, 8, 18912−18921.

(53) Yousef, R.; El-Eswed, B.; lL-Muhtaseb, A. Adsorption characteristics of natural zeolites as solid adsorbents for phenol removal from aqueous solutions: Kinetics, mechanism, and thermodynamics studies. *Chem. Eng. J*. **2011**, 171, 1143–1149.

(54) Azizian, A. Kinetic models of sorption: a theoretical analysis. *J. Colloid Interface Sci*. **2004**, 276, 47–52.

(55) Aroua, M.; Leong, S.; Teo, L.; Yin, C-Y.; Daud, W. Real-time determination of kinetics of adsorption of lead (II) onto palm shell-bases activated carbon using ion selective electrode. *Bioresour. Technol*. **2008**, 99, 5786–5792.

(56) Camacho, L.; Parra, R.; Deng, S. Arsenic removal from groundwater by MnO_2-modified natural clinoptilolite zeolite: Effects of pH and initial feed concentration. *J. Hazard. Mater*. **2011**, 189, 286–293.

(57) Baltazar, S.E.; García, A.; Romero, A. H.; Rubio, M. A.; Arancibia-Miranda N.; Altbir, D. Surface rearrangement of nanoscale zerovalent iron: the role of pH and its implications in the kinetics of arsenate sorption. *Environ. Technol*. **2014**, 35 (18), 1–8.

(58) Vitos, L.; Ruban, A.V.; Skriver, H.L.; Kollár, J. The surface energy of metals. *Surf. Sci.* **1998**, 186–202.

(59) Thant Zin, M.; Borja, J.; Hinode, H.; Kurniawan, W. Synthesis of Bimetallic Fe/Cu Nanoparticles with Different Copper Loading Ratios. *WASET. International Journal of*

Chemical, Molecular, Nuclear, Materials and Metallurgical Engineering **2013**, 7 (12), 1031–1035.

(60) Ha Tran, T.; Tuyen Nguyen, V. Copper Oxide nanomaterials prepared by solution methods, some properties, and potential applications: A brief review. *Int. Sch. Res. Notices* **2014**, 2014, 1–14.

(61) J. Siegfried, M.; Choi, K-S. Electrochemical crystallization of cuprous oxide with systematic shape evolution. *Adv. Mater.* **2014**, 16 (19), 1743–1746.

(62) Condi de Godoia, F.; Balloni, R.; Aparecida, M.; Rodriguez, E.; Guibal, E. Masumi, M. Introduction of copper nanoparticles in chitosan matrix as strategy to enhance chromate adsorption. *Chem. Eng. Process.* **2014**, 83, 43–48.

(63) González, A.; Moreno, N.; Navia, R.; Querol, X. Study of a Chilean petroleum coke fluidized bed combustion fly ash and its potential application in copper, lead and hexavalent chromium removal. *Fuel* **2010**, 89(10), 3012–3021.

(64) Sh Ho, Y. Review of second-order models for adsorption systems. *J. Hazard. Mater.* **2006**, 136, 681–689.

(65). Martinson, C. A.; Reddy, K. J. Adsorption of arsenic(III) and arsenic(V) by cupric oxide nanoparticles. *J. Colloid Interface Sci.* **2009**, 336, 406–411.

(66) Goswamia, A.; P.K. Raul, P. K.; Purkaita, M.K. Arsenic adsorption using copper (II) oxide nanoparticles. *Chem. Eng. Res. Des.* **2012**, 90, 1387–1396.

(67) de Godoi, F.; Rodriguez-Castellon, E.; Guibal, E.; Masumi, M. An XPS study of chromate and vanadate sorption mechanism by chitosan membrane containing copper nanoparticles. *Chem. Eng. J.* **2013**, 234, 423–429.

(68) de Godoi, F.; Balloni, R.; Silva, M. A.; Rodríguez-Castellón, E.; Guibal, E.; Masumi, M. Introduction of copper nanoparticles in chitosan matrix as strategy to enhance chromate adsorption. *Chem. Eng. Process* **2014**, 83, 43–48.

(69) Shaolin Li, S.; Wang, W.; Liu, Y.; Zhang, W. Zero-valent iron nanoparticles (nZVI) for the treatment of smelting wastewater: A pilot-scale demonstration. *Chem. Eng. J.* **2014**, 254, 115–123.

(70) Li, S.; Wang, W.; Liang, F.; Zhang, W. Heavy metal removal using nanoscale zero-valent iron (nZVI): Theoryand application. *J. Hazard. Mater*. **2017**, 322,163–171.

(71) Yan, W.; Vasic, R.; Frenkel, A.; Koel, B. Intraparticle Reduction of Arsenite (As(III)) by Nanoscale ZerovalentIron (nZVI) Investigated with In Situ X-ray Absorption Spectroscopy. *Environ. Sci. Technol*. **2012**, 46, 7018–7026.

FIGURE CAPTIONS

Figure 1. Partial binding energy of the FeCu clusters as a function of Cu concentration. Four initial configurations were considered: Core-Shell (CS), Polycrystals (PL), Segregated (SG), and Isolated (IS). The inset shows a zoomed view of the binding energy per atom.

Figure 2. (a) Total and partial RDF of the FeCu clusters at different Cu concentrations. The right side shows the relaxed cluster configurations of (b) $Fe_{0.9}Cu_{0.1}$ and (c) $Fe_{0.5}Cu_{0.5}$. Fe and Cu atoms are depicted as orange and green particles, respectively.

Figure 3. (a) Linear atomic distribution of Fe and Cu in simulated FeCu BMNPs at two Cu concentrations. The yellow lines in (b) and (c) show the linear mapping of each particle at $Fe_{0.9}Cu_{0.1}$ and $Fe_{0.5}Cu_{0.5}$, respectively.

Figure 4. Magnetic hysteresis of the BMNPs. The graph shows the magnetic behavior at room temperature of the FeCu BMNPs as a function of the Cu concentration and the monometallic nanoparticles. The inset shows the low magnetic field for better comparison (same units as in the main figure).

Figure 5. XRD of (a) nZVI, (b) $Fe_{0.9}Cu_{0.1}$, (c) $Fe_{0.5}Cu_{0.5}$, and (d) Cu NPs. Symbols: ($\bullet$) = Fe^0, ($\blacktriangle$): Cu^0, ($\blacksquare$) = cuprite, ($\blacktriangledown$) = tenorite, and ($\blacktriangleleft$) = magnetite.

Figure 6. Pre-sorption SEM micrographs of (a) nZVI, (b) $Fe_{0.9}Cu_{0.1}$, (c) $Fe_{0.5}Cu_{0.5}$, and (d) Cu NPs; and post-sorption of (e) nZVI-As, (f) $Fe_{0.9}Cu_{0.1}$-As, (g) $Fe_{0.5}Cu_{0.5}$-As, and (h) Cu NPs-As. Symbols: ○ nZVI agglomerates; ○: Cu agglomerates; and ○: sheets. Images at different scales.

Figure 7. TEM images of (a) nZVI, b) $Fe_{0.9}Cu_{0.1}$, c) $Fe_{0.5}Cu_{0.5}$, and d) Cu NPs before As sorption; (e) $Fe_{0.9}Cu_{0.1}$ after As sorption; and (f) the atomic structure of BMNPs ($Fe_{0.9}Cu_{0.1}$) with the characteristic (110) planes of the bcc phase Fe (i, ii and iii).

Figure 8. Linear mapping of FeCu BMNPs. The concentration profiles of the $Fe_{0.9}Cu_{0.1}$ samples (a) before As sorption, showing Fe particles. (b) and (c) show the larger particles obtained after As sorption due to oxidation of the Fe and Cu NPs. The concentration profiles of the $Fe_{0.5}Cu_{0.5}$ samples in (d) and (e) before and in (f) and (g) after As sorption denote the presence of Fe and Cu NPs and Fe and Cu oxides with As concentrations.

Figure 9. Arsenate removal studies: (a) sorption kinetics and (b) sorption isotherms. Symbols: (■) nZVI; (▲) $Fe_{0.9}Cu_{0.1}$; (◄) $Fe_{0.5}Cu_{0.5}$; (●) Cu NPs; and (---) better fit models, i.e., the PSO and *Freundlich* models, for the sorption kinetics and isotherms, respectively.

Figure 10. Proposed mechanism of As(V) removal using bimetallic materials as the adsorbent.
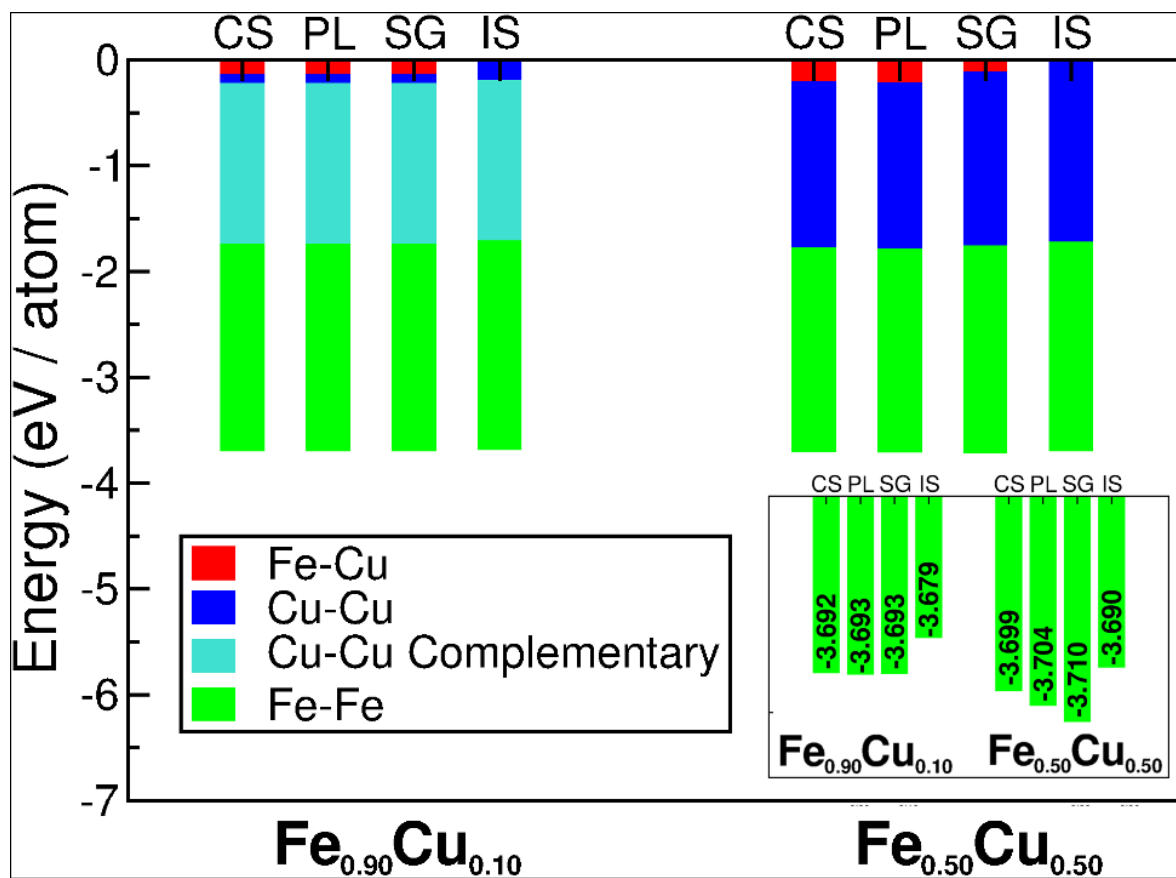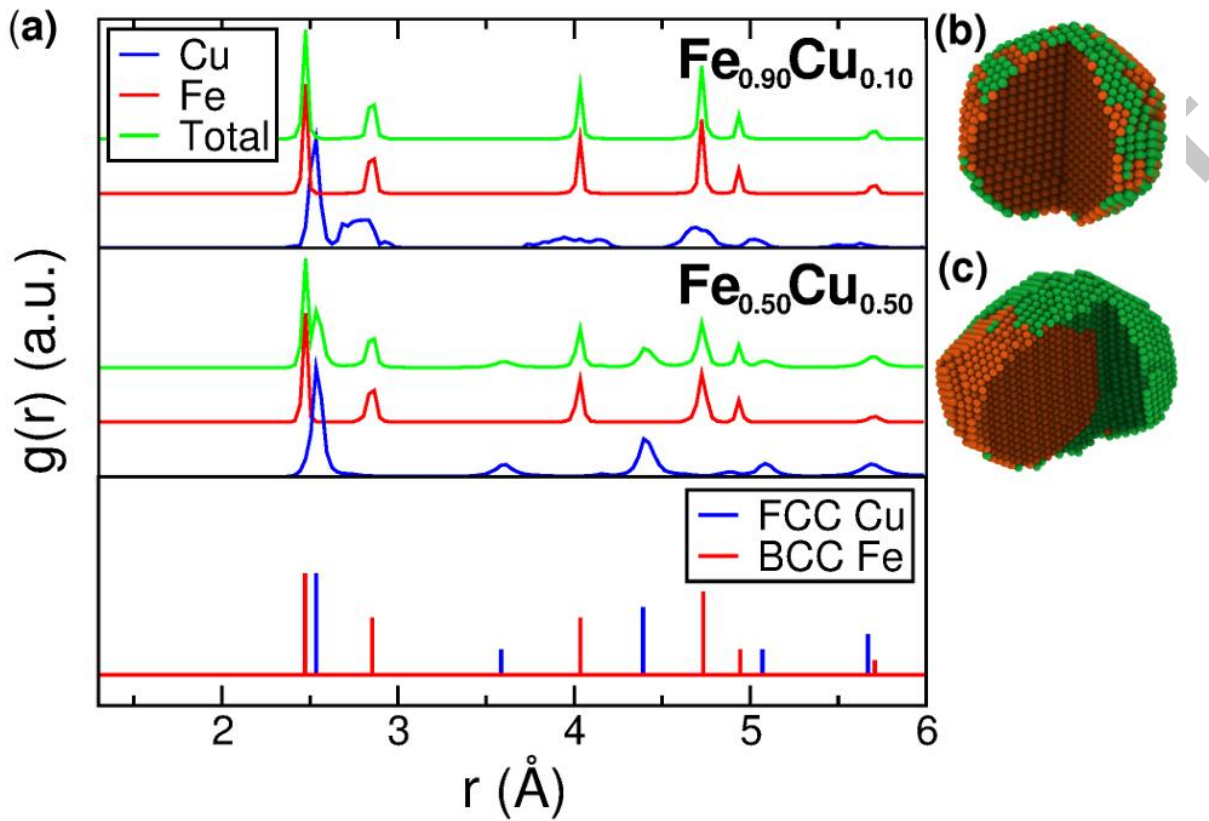
Figure 1

Figure 2

Figure 3
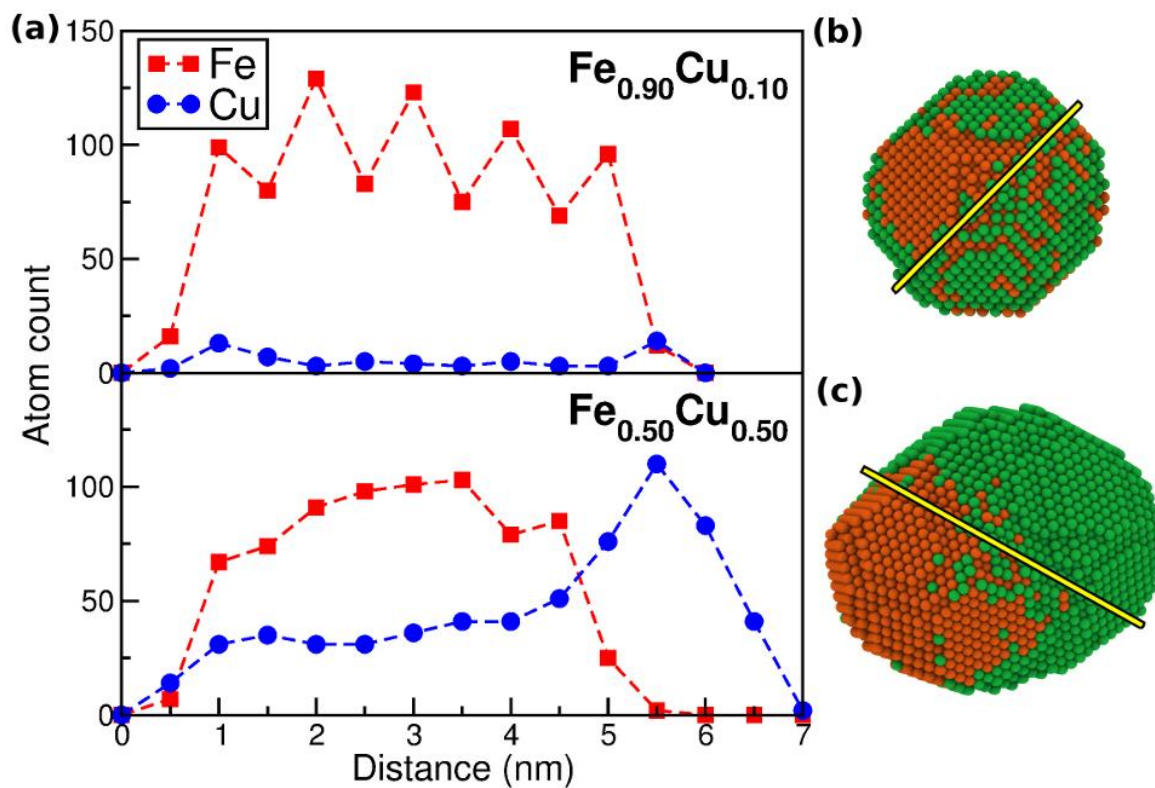
Figure 4
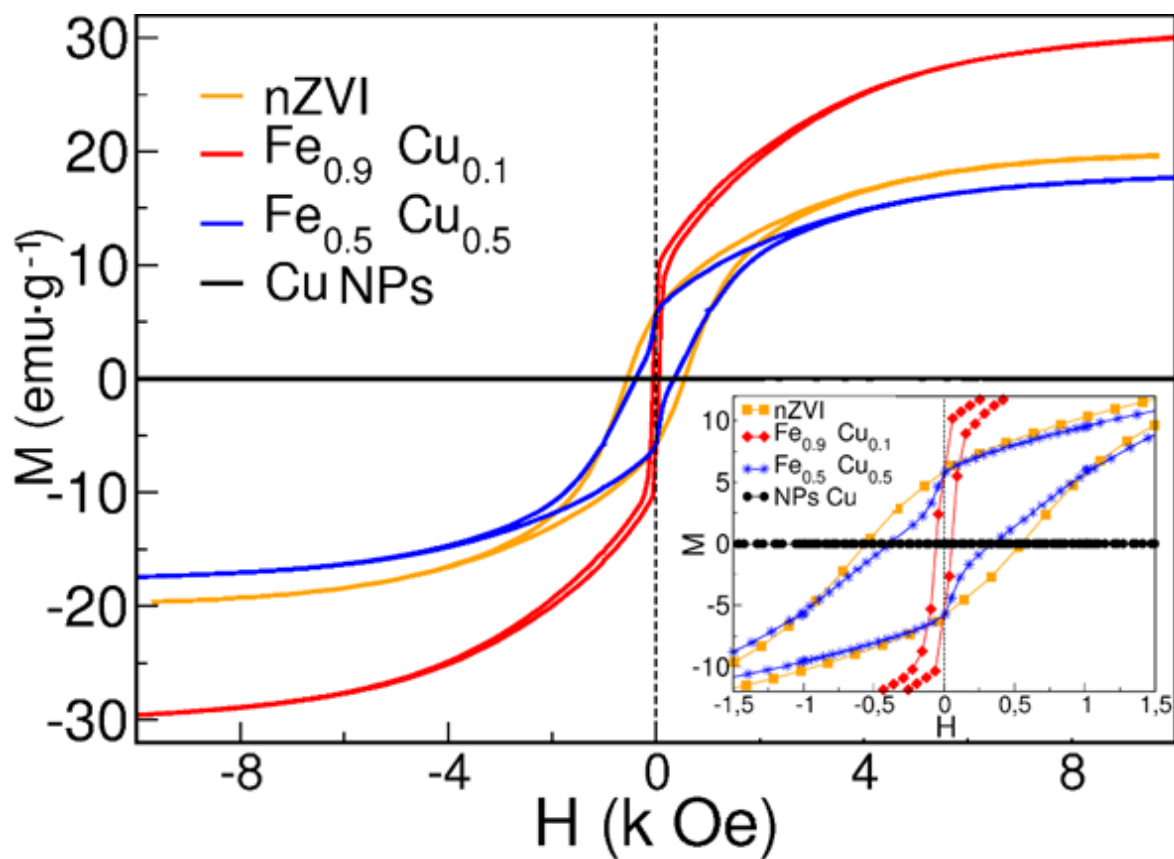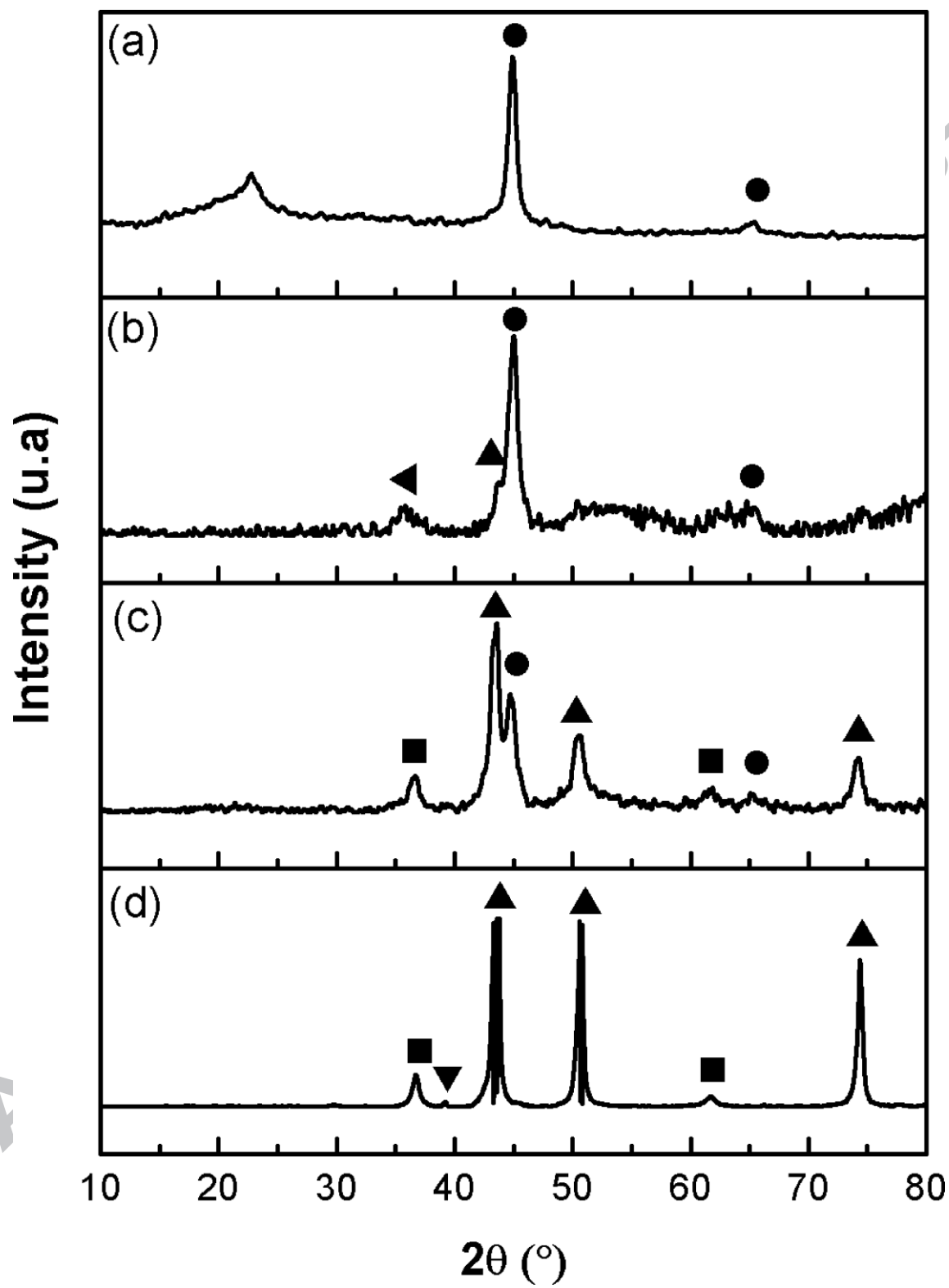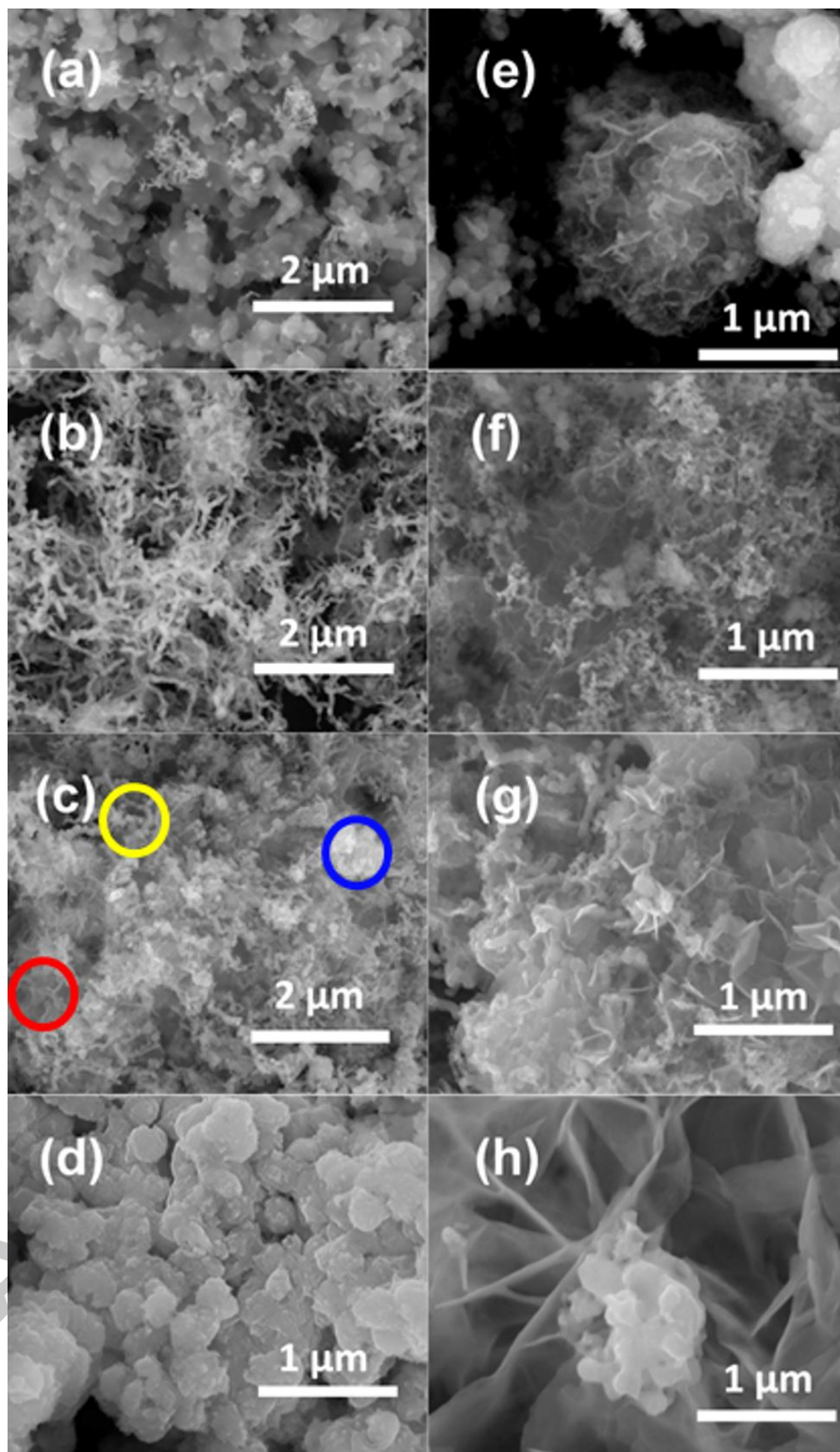
Figure 5

Figure 6

Figure 7
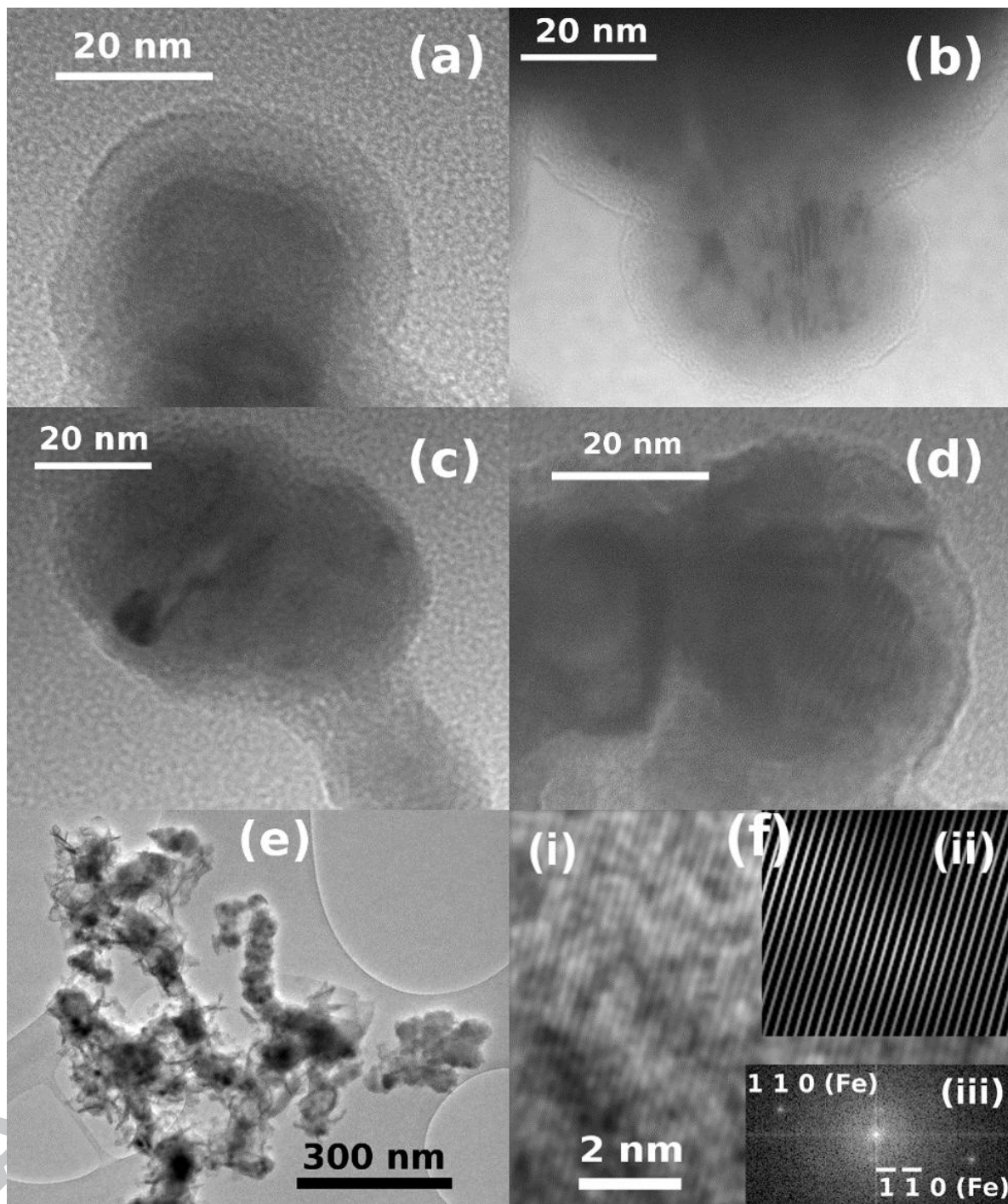
Figure 8
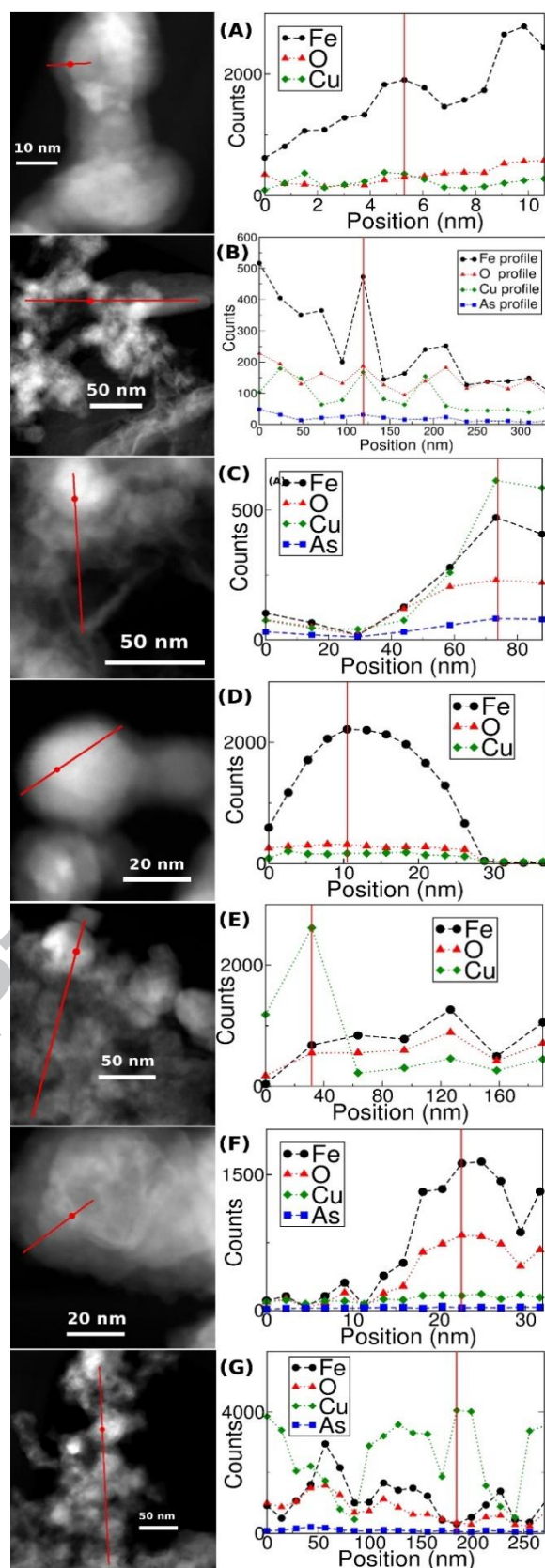
Figure 9
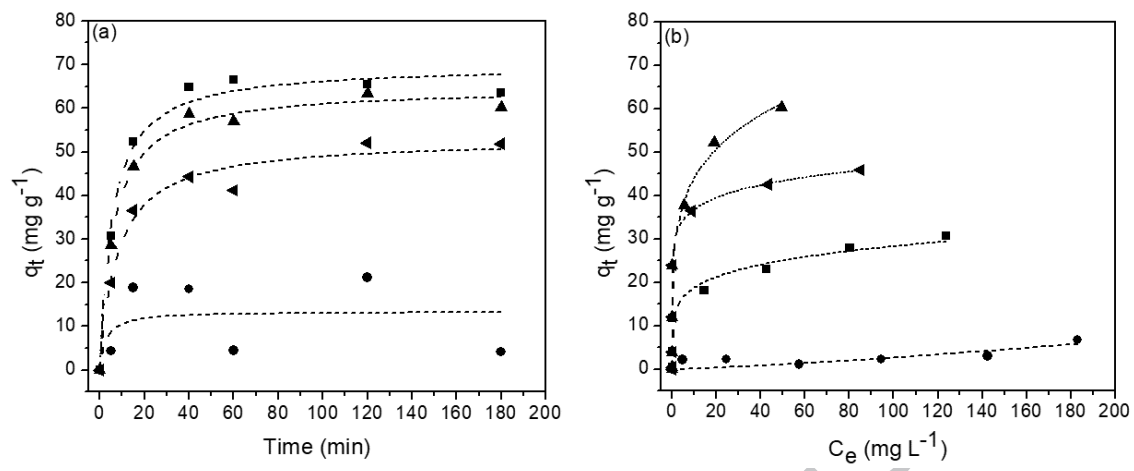
Figure 10
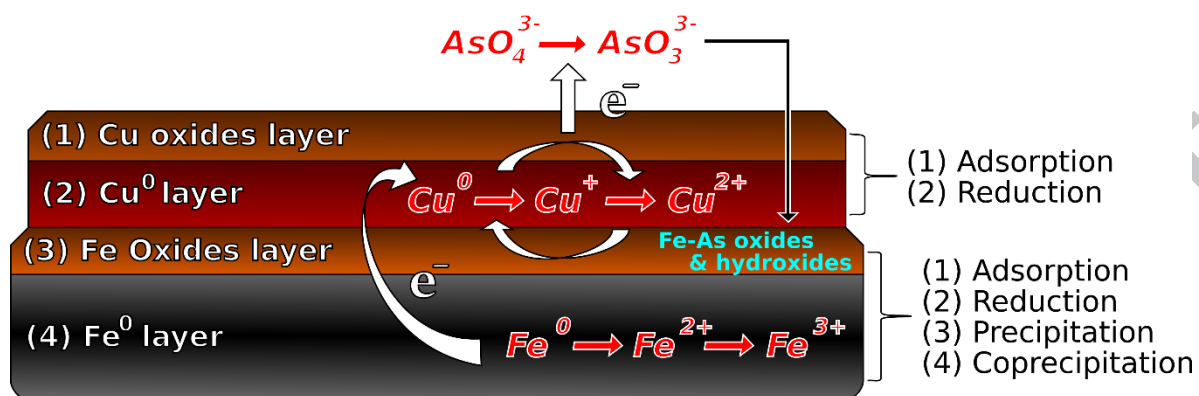
Table 1. *Pseudo-first-order (PFO) and pseudo-second-order (PSO) statistical and kinetic parameters obtained for the removal of AS(V) using five adsorbent materials.*

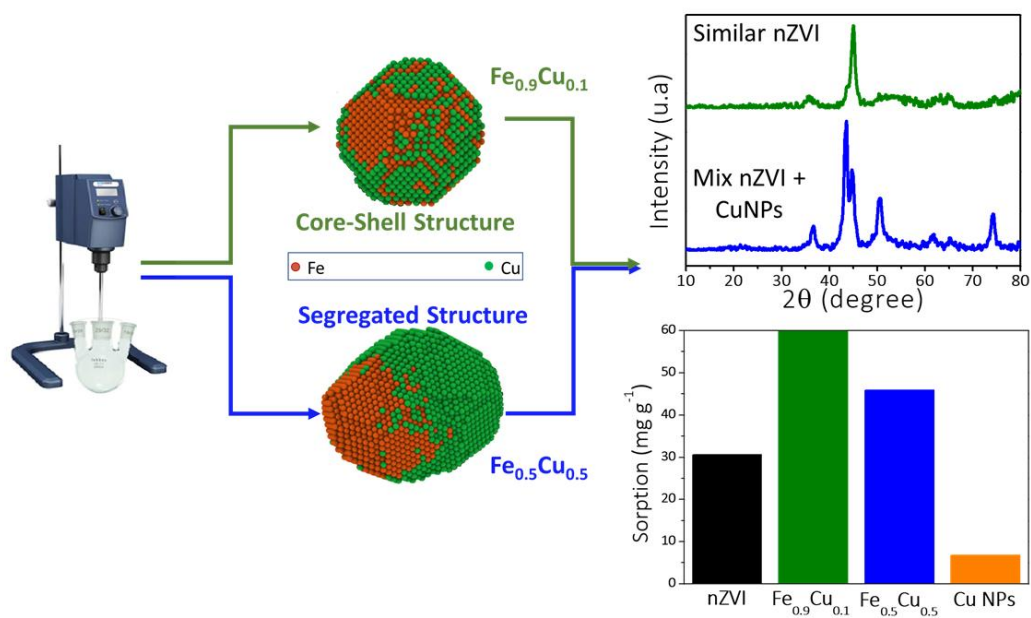| Parameters	As^V			
	nZVI	Fe$_{0.9}$Cu$_{0.1}$	Fe$_{0.5}$Cu$_{0.5}$	Cu NPs
$q_{exp}(mg \cdot g^{-1})$	63.58	60.179	58.098	4.130
$q_{exp}(\%)$	79.860	75.223	72.767	5.147
Pseudo-Second-Order				
$q_e(mg \cdot g^{-1})$	69.740	64.584	60.832	N.D
$k_2(*10^{-3} g \cdot mg^{-1} \cdot min^{-1})$	2.000	2.600	2.000	N.D
$h(mg \cdot g^{-1} \cdot min^{-1})$	9.727	10.845	7.401	N.D
r^2	0.986	0.993	0.997	N.D
RMSE	2.322	1.011	0.627	N.D
X^2	0.597	0.322	0.129	N.D

N.D: Not determined.

Table 2. Statistical and *Freundlich* sorption isotherm parameters for the sorption of As(V) using five adsorbent materials.

Parameters	As^V			
	nZVI	$Fe_{0.9}Cu_{0.1}$	$Fe_{0.5}Cu_{0.5}$	Cu NPs
$q_{exp}(mg \cdot g^{-1})$	30.595	60.220	55.015	6.723
Freundlich				
K_F	12.513	27.341	30.752	1.312
n	5.644	4.842	7.000	9.819
r^2	0.970	0.782	0.755	0.623

Graphical abstract